

Article

Correcting Forecast Time Biases in CMA-MESO Using Himawari-9 and Time-Shift Method

Xingtao Song^{1,2}, Wei Han^{3,4,*} , Haofei Sun^{5,6}, Hao Wang^{3,4} and Xiaofeng Xu^{1,2}

¹ School of Atmospheric Physics, Nanjing University of Information Science and Technology, Nanjing 210044, China; 202312030051@nuist.edu.cn (X.S.); xxf@nuist.edu.cn (X.X.)

² Key Laboratory for Aerosol-Cloud-Precipitation of China Meteorological Administration, School of Atmospheric Physics, Nanjing University of Information Science and Technology, Nanjing 210044, China

³ CMA Earth System Modeling and Prediction Centre (CEMC), China Meteorological Administration, Beijing 100081, China; wanghao@cma.gov.cn

⁴ State Key Laboratory of Severe Weather (LaSW), Chinese Academy of Meteorological Sciences, China Meteorological Administration, Beijing 100081, China

⁵ State Key Laboratory of Atmospheric Boundary Layer Physics and Atmospheric Chemistry (LAPC), Institute of Atmospheric Physics, Chinese Academy of Sciences, Beijing 101408, China; sunhaofei20@mailsucas.ac.cn

⁶ University of Chinese Academy of Sciences, Beijing 101408, China

* Correspondence: hanwei@cma.gov.cn

Abstract: The accurate forecasting of time, intensity, and spatial distribution is fundamental to weather prediction. However, the limitations of numerical weather prediction (NWP) models, as well as uncertainties in initial conditions, often lead to temporal biases in forecasts. This study addresses these biases by employing visible reflectance data from the Himawari-9/AHI satellite and RTTOV (TOVS radiation transfer) simulations derived from CMA-MESO model outputs. The time-shift method was applied to analyze two precipitation events—20 October 2023 and 30 April 2024—in order to assess its impact on precipitation forecasts. The results indicate the following: (1) the time-shift method improved cloud simulations, necessitating a 30 min advance for Case 1 and a 3.5 h delay for Case 2; (2) time-shifting reduced the standard deviation of observation-minus-background (OMB) bias in certain regions and enhanced spatial uniformity; (3) the threat score (TS) demonstrated an improvement in forecast accuracy, particularly in cases exhibiting significant movement patterns. The comparative analysis demonstrates that the time-shift method effectively corrects temporal biases in NWP models, providing forecasters with a valuable tool to optimize predictions through the integration of high-temporal- and spatial-resolution visible light data, thereby leading to more accurate and reliable weather forecasts.

Keywords: Himawari-9; CMA-MESO; time shift



Academic Editor: Yuriy Kuleshov

Received: 30 December 2024

Revised: 8 February 2025

Accepted: 10 February 2025

Published: 11 February 2025

Citation: Song, X.; Han, W.; Sun, H.; Wang, H.; Xu, X. Correcting Forecast Time Biases in CMA-MESO Using Himawari-9 and Time-Shift Method. *Remote Sens.* **2025**, *17*, 617. <https://doi.org/10.3390/rs17040617>

Copyright: © 2025 by the authors. Licensee MDPI, Basel, Switzerland. This article is an open access article distributed under the terms and conditions of the Creative Commons Attribution (CC BY) license (<https://creativecommons.org/licenses/by/4.0/>).

1. Introduction

Data assimilation (DA) and numerical weather prediction (NWP) constitute the primary methods employed in contemporary weather forecasting. With the increasing availability of observational data, improved computational performance, and the rapid development of numerical models, the accuracy and resolution of weather forecasts have seen substantial improvements. However, inherent model flaws and uncertainties in initial conditions still lead to forecast errors [1]. Even high-resolution regional models cannot fully resolve these issues. Conventional observational data are limited by spatial and temporal resolution and coverage, while ground-based observations are relatively sparse, making it

difficult to meet the spatial and temporal density requirements necessary for initializing numerical weather prediction models. Satellite remote sensing observations, with extensive temporal and spatial coverage, can overcome these limitations [2]. Satellite data now contribute more to forecast accuracy than conventional ground-based observations [3]. By assimilating both conventional and unconventional data from sources like satellites and radar, numerical forecasts can be significantly improved, yielding more accurate forecasting outcomes. The Global/Regional Assimilation and Prediction System (GRAPES), now renamed CMA-MESO, developed under the auspices of the China Meteorological Administration, has made significant advancements in key NWP technologies, such as satellite data assimilation and scalable numerical algorithms [4]. Recent verification and evaluation studies have shown promising results, with research focused on assessing the performance of various regional models and precipitation diagnostic methods, significantly contributing to the enhancement of precipitation prediction capabilities. Specifically, Tong et al. [5], Zhang et al. [6], and Fan et al. [7] conducted studies on regional models and precipitation-phase prediction methods, proposing several improvements that enhanced the accuracy of precipitation predictions. Additionally, Liu et al. evaluated the performance of the CMA-MESO and the Shanghai Regional Mesoscale Numerical Weather Prediction System (CMA-SH9) using precipitation data from the extended Meiyu season (May to September) of 2020. Their results indicated that the CMA-MESO ranked second or third in terms of TS, and its Bias Score (BIAS) was close to 1 in most cases, highlighting its superior capability to predict the precipitation range, with the second-best performance overall [8]. Wan et al., evaluated CMA-MESO during the Henan extreme rainfall event in July 2021. The results showed that the model effectively predicted the shape of the rainfall band, the duration of weak echoes, and the area and intensity evolution of the major convective systems (MCSs) before and after the peak precipitation period [9].

Compared to longwave (infrared) and microwave radiation, shortwave radiation remains underutilized in NWP [10–12]. This is due to significant OMB differences, a consequence of the complex sensor sensitivities to clouds, aerosols, and surface features, the limitations in modeling complex cloud processes, and several other contributing factors [13]. Additionally, shortwave observations are limited to daytime, which further restricts their applicability [3]. However, visible-wavelength observations provide valuable information on clouds (especially low-level clouds) and aerosols, because the clear atmosphere minimally absorbs shortwave radiation, providing an advantage over infrared and microwave data [14–16]. Visible channels can help distinguish between cirrus and high cumulus clouds, crucial for improving initial conditions in cloudy and precipitation regions to enhance NWP capabilities [17]. In the visible spectrum, scattering and absorption by molecules, water droplets, ice crystals, and aerosol particles play significant roles. Polar-orbiting satellites typically observe a given location twice per day at lower latitudes, which limits their ability to provide high-temporal-frequency observations. In contrast, geostationary satellites, such as Himawari, maintain a consistent temporal resolution across latitudes by performing full-disk scans every 10 min, ensuring continuous hemispheric coverage. Schrötle et al. found that combining visible and infrared satellite radiances significantly improved precipitation forecasts within an 8 h lead time [18]. Scheck et al. demonstrated that assimilating visible reflectance improved cloud cover and reduced temperature and humidity errors [19]. Stefan et al., emphasized the usefulness of visible channels for model evaluation and improvement through comparisons in observation space using synthetic satellite images generated by forward operators [20]. Accurate radiative transfer models like RTTOV (radiative transfer for TOVS) can simulate visible observations under scattering conditions. Comparing simulated and satellite images can reveal discrepancies in both RTTOV and weather forecast models [21,22].

Accurate prediction of the timing, intensity, and location of weather phenomena necessitates the simultaneous consideration of all three factors. However, due to inherent limitations in numerical weather prediction models and uncertainties in initial conditions, forecasts often exhibit time biases (i.e., the forecasted results occur either too early or too late compared to actual conditions) [8,23,24]. Such time biases can significantly affect the accuracy of weather forecasts. For instance, Cai et al. [25] evaluated precipitation forecasts from the CMA-MESO model during the summer of 2021 and found that while the forecast frequencies of 3 h precipitation in the complex terrain of western Sichuan were relatively close to the observations, the forecasted precipitation amounts were less accurate, and the peak precipitation occurred too early. Similarly, Chen et al. [26] pointed out that the precipitation forecast frequencies in South and East China were much higher than observed, especially for nighttime precipitation, which was notably overestimated. To investigate this issue, the present study utilizes visible channel data from the Himawari-9/AHI satellite and RTTOV-simulated results from CMA-MESO to correct time biases in precipitation forecasts for China using the time-shift method. The primary objective of this study is to demonstrate the effectiveness of the time-shift method in correcting time biases, while offering new insights into reducing forecast discrepancies by incorporating visible reflectance data. Moreover, this method holds significant practical value for forecasters. By leveraging the high temporal resolution and extensive spatial coverage of data from geostationary satellites, forecasters can assess model forecast results in real time and make necessary adjustments. This improves the accuracy of timing predictions for weather phenomena. Such adjustments can substantially enhance the precision, reliability, and applicability of weather forecasts, enabling regions to better prepare for upcoming weather events.

2. Materials and Methods

2.1. Schema

In operational weather forecasting, the CMA-MESO model is initiated at time T_0 , where the forecaster receives the model output at time T_1 and issues the final forecast at time T_2 (Figure 1). Due to the inherent limitations of numerical weather prediction models and uncertainties in the initial conditions, forecasts may exhibit deviations in terms of timing, intensity, and spatial location. Therefore, during the period between T_1 and T_2 , when forecasters conduct potential and error analyses, they may identify temporal biases in the model output (such as forecasts being too early or too late). In such cases, high-temporal-resolution and wide-spatial-coverage satellite data, such as Himawari-9 albedo data, can be used to evaluate and correct the model's predictions, resulting in more accurate forecasts by T_2 , thus enhancing overall forecast accuracy. This paper proposes a time-shifting method, where actual satellite imagery is compared and matched with simulated observations from adjacent time periods to identify the time that minimizes the difference between observation and simulation (i.e., minimizes the OMB), thus refining the forecast outcomes. This method provides forecasters with an innovative method for correcting the model's time bias between T_1 and T_2 .

2.2. Radar Composite Reflectivity

Radar Composite Reflectivity (CREF, dBZ) is the measurement of radar waves reflected by clouds at various altitudes within a defined range of the meteorological radar. It is utilized for estimating cloud thickness and height, as well as predicting severe convective weather events, such as intense rainfall and storms. This study examined two precipitation events and employed Radar Composite Reflectivity data to elucidate the characteristics and evolution of the precipitation processes.

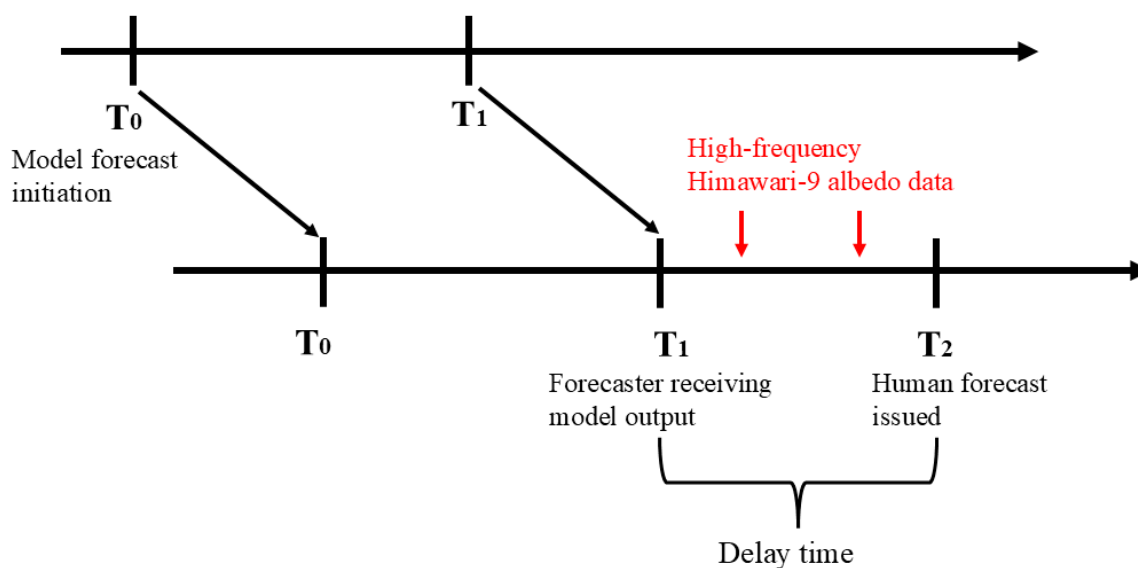


Figure 1. Schematic of CMA-MESO numerical weather prediction model.

2.3. Precipitation Integration Products

The National Meteorological Information Center has issued the CMA Multi-source Precipitation Analysis System (CMPAS) hourly precipitation fusion analysis product, featuring a spatial resolution of $0.05^\circ \times 0.05^\circ$. This product corrects systematic biases in radar-estimated and satellite-derived precipitation using the Probability Density Function Matching method. Subsequently, the Bayesian Model Averaging (BMA) technique is employed to merge radar and satellite precipitation products, forming a background field covering China. Finally, ground observation data are integrated using Optimal Interpolation [27]. The system dynamically calculates errors from various data sources within different spatiotemporal windows, assigning weights that vary across regions and times, thereby enhancing the accuracy of local weight distribution. CMPAS encompasses nine components: data acquisition, data preprocessing, data fusion, product generation, product evaluation, product dissemination, system monitoring, data management, and operational scheduling. It can sequentially generate various 1 km and 5 km precipitation fusion data and graphical products based on the timeliness requirements for product generation, along with real-time quality assessment results. In this study, the precipitation product data were primarily utilized as observed precipitation data.

2.4. CMA-MESO

The Global/Regional Assimilation and Prediction Enhanced System (GRAPES), developed by the China Meteorological Administration, is a numerical prediction and data assimilation system that began development in 2001, and was first operationally implemented in 2006. With continuous updates to its versions, the horizontal resolution has improved from 30 km in 2006 to 3 km in 2021. On 1 October 2021, GRAPES-MESO was renamed CMA-MESO.

CMA-MESO, built upon international research findings and numerical weather prediction principles, is a numerical prediction model with a uniform latitude–longitude grid. The operational system consists of three main components: the observational data preprocessing subsystem, the main model subsystem, and the postprocessing subsystem. The observational data preprocessing subsystem includes a radar data preprocessing module (mosaic_v4) and other data retrieval modules (obs_rafs). The main model subsystem comprises several modules: global forecast data preprocessing, observational data preprocessing (including conventional radiosonde, surface, aircraft, ship, cloud-drift wind, radar

radial wind, wind profiler radar, and GPS/PW observations), data assimilation, and model forecasting. The postprocessing subsystem includes diagnostic calculation modules and graphical product generation modules.

The data assimilation employs the GRAPES global-regional integrated variational assimilation system, with the regional model utilizing a three-dimensional variational assimilation option. The forecast region covered 10.0°N to 60.01°N and 70.0°E to 145.0°E, with a spatial resolution of 0.03° (approximately 3 km). The model consisted of 50 layers, extending up to 33,000 m (10 hPa). The model output variables included height, temperature, precipitation, and the mixing ratios of cloud water, rainwater, ice crystals, snow, and graupel. The dynamical framework was based on fully compressible primitive equations, a semi-implicit semi-Lagrangian time integration scheme, an Arakawa-C grid on a uniform latitude–longitude grid, and vertical terrain-following coordinates [28]. The model provided forecast results for up to 36 h.

2.5. Himawari-9

Himawari-9, launched by the Japan Meteorological Agency (JMA), is a third-generation geostationary meteorological satellite equipped with the Advanced Himawari Imager (AHI), one of the most advanced geostationary imagers in the world. The AHI on Himawari-9 completes a scan every 10 min, covering five regions: the full disk (the entire Earth as seen from the satellite), the Japan area, the target area, and two landmark areas. The AHI offers significantly higher spectral and spatial resolution than the previous generation of geostationary satellites, with 16 observational channels that greatly enhance cloud-detection capabilities (Table 1). This provides an enhanced and highly effective tool for mesoscale weather monitoring and forecasting. The channel near 0.65 μm is commonly used to monitor cloud information [29]. Thus, this study focused on the third channel (0.64 μm) of the Himawari-9 satellite.

Table 1. Himawari-9/AHI instrument channel parameters.

Spectrum	Channel	Central Wavelength/ μm	Spatial Resolution/km
Visible	1	0.47	1
	2	0.51	1
	3	0.64	0.5
Near-infrared	4	0.86	1
	5	1.6	2
	6	2.3	2
Infrared	7	3.9	2
	8	6.2	2
	9	6.9	2
	10	7.3	2
	11	8.6	2
	12	9.6	2
	13	10.4	2
	14	11.2	2
	15	12.4	2
	16	13.3	2

In this study, we used Level 1 NC (Network Common Data Format) full-disk observations from the Himawari-9 meteorological satellite (Table 2), including satellite zenith angle (SAZ), azimuth angle (SAA), solar zenith angle (SOZ), azimuth angle (SOA), and visible channel albedo data. These data were calibrated and atmospherically corrected, making them ready for direct use.

Table 2. Himawari L1 grid data.

Data Type	Full Disk
Projection method	EQR
Observation area	60°S–60°N, 80°E–160°W
Time resolution	10 min
Data	Albedo of Bands 01–06 Brightness temperature of Bands 07–16 SOZ; SOA; SAZ; SAA Observation Hours (UT)

2.6. RTTOV

RTTOV (radiative transfer for TOVS) is a fast radiative transfer model initially designed for the TIROS Operational Vertical Sounder (TOVS) instruments aboard NOAA polar-orbiting satellites, based in Washington, USA [14]. Over time, the applicability of RTTOV has expanded to various satellite instruments, enabling the simulation of top-of-atmosphere radiance for passive visible, infrared, and microwave downward-looking satellite radiometers. A key feature of the RTTOV model is its ability to perform not only forward (direct) radiative transfer calculations but also compute tangent linear, adjoint, and Jacobian matrices. These matrices provide the radiative response to perturbations in the profile variables, assuming a linear relationship for a given atmospheric state. Given a state vector x , the radiative vector y is computed as

$$y = H(x) \quad (1)$$

where H represents the radiative transfer model (also known as the observation operator). Fast radiative transfer models are critical for satellite remote sensing atmospheric parameter retrievals and the direct assimilation of satellite radiance data, and they have been widely used in operational meteorological satellite retrieval products and numerical weather prediction both domestically and internationally [30], demonstrating significant success.

In this study, the optical properties of liquid water clouds were parameterized using the “Deff” scheme [31], while the optical properties of ice clouds were computed using the cirrus scheme developed by Baran et al., which is not explicitly dependent on ice particle size [32]. Therefore, this scheme simplified the analysis of results, and the effective radius of ice particles was excluded from further analysis. The effective particle radius of liquid water can be approximated using the liquid water cloud mixing ratio q_w and concentration N_w , as per Thompson et al. [22,33]:

$$R_w = \frac{1}{2} \times \left(\frac{6\rho_a q_w}{\pi\rho_w N_w} \right)^{\frac{1}{k}} \quad (2)$$

where ρ_a and ρ_w are the densities of the air and liquid water cloud particles, respectively. ρ_a is obtained from the equation of state, while ρ_w and N_w are constants set to 1000 kg/m³ and 300 cm³, respectively. The constant k is set to 3.

When simulating visible channel reflectance with the RTTOV model, atmospheric state variables needed to be collected to gather information regarding the location, surface type, and atmospheric conditions (Table 3). These data were subsequently entered into the Bidirectional Reflectance Distribution Function (BRDF). Using the satellite’s position and Coordinated Universal Time (UTC), key parameters including the solar zenith angle, solar azimuth angle, satellite zenith angle, and satellite azimuth angle were determined. Once the simulation scene was set, it was entered into the RTTOV model to generate simulated outcomes.

Table 3. Initial variables for RTTOV input.

Variable Types	Variables	Units
Profile Variables	Temperature	K
	Pressure	hPa
	Water Vapor	kg/kg
	Cloud Liquid Water Content	kg/kg
	Cloud Ice Water Content	kg/kg
	Total Cloud Cover	
	Effective Radius of Liquid Water Cloud Particles	μm
Surface Parameters	2m Surface Temperature	K
	2m Surface Pressure	hPa
	10m U and V Wind Components	m/s
	Surface Temperature	K
	Surface Pressure	hPa
	Terrain Height	m
	Surface Type	
Satellite Parameters	Solar Azimuth Angle (SOA)	°
	Solar Zenith Angle (SOZ)	°
	Satellite Azimuth Angle (SAA)	°
	Satellite Zenith Angle (SAZ)	°

2.7. NWP Model Time Shifts

Forecasts may exhibit time biases in certain cases due to the limitations of numerical weather prediction models and the uncertainty of the initial field. This study investigated the potential of high-temporal-resolution visible data from geostationary satellites in correcting forecast-time biases by examining two cases. One case involved Typhoon Sanba, where a time bias in the model forecast was identified during the 0000 UTC weather briefing on 20 October 2023, and the corresponding time was chosen for analysis. The second case involved a squall line that fully developed at 0220 UTC on 30 April 2024, but the model forecast was issued later than anticipated, making this time the focus of the study. Both cases were provided by the Central Weather Bureau. This study utilized high-temporal-resolution Himawari-9 satellite data to compare and align actual satellite images with simulated observations from neighboring time intervals, identifying the time point that minimized the difference between observation and simulation (i.e., the time-shift method). This correction method enables forecasters to adjust the forecast prior to manual release, thereby improving forecast accuracy.

Since correlation was primarily dependent on the similarity in the shape, size, and location of clouds between the observed and simulated data, this study employed correlation as the criterion for determining the optimal time shift. The optimal time shift, $\Delta t_{optical}$, was defined as the time when the correlation was maximized, i.e., when $\Delta t_{optical} = r_{max}$.

Additionally, the Himawari-9 satellite data incorporates real atmospheric changes, such as friction, energy dissipation, and vertical transport, with a data interval of 10 min. Consequently, the time-shift increment was set to 10 min. To maximize the search space and optimize the use of available data, the time-shift window was defined as 6 h. Furthermore, to avoid errors induced by variations in temperature, humidity, and other factors that may alter the albedo in clear-sky areas (since Taiwan is a clear-sky area, this effect is not considered), this study initially defined the study area based on observed visible cloud images. Given that the locations of the two precipitation events differed, the areas considered for the two cases varied slightly. Subsequently, terrestrial albedo was extracted using a sea–land mask to reduce external errors.

The correlation formula is as follows:

$$r = \frac{\sum (X_i - \bar{X})(Y_i - \bar{Y})}{\sqrt{\sum (X_i - \bar{X})^2 \sum (Y_i - \bar{Y})^2}} \quad (3)$$

where X_i and Y_i represent the i th simulated and observed albedo data points, and \bar{X} and \bar{Y} are the mean values of the simulated and observed albedo data, respectively.

2.8. Methods for Analyzing Errors

To further investigate the effect of time shifts, this study compared the probability density function (PDF) distribution and spatial distribution of the OMB before and after the time shifts. The PDF is a key tool for describing the probability distribution of continuous random variables. It visually illustrates the distribution pattern of the variable of interest. The mean determines the central location of the distribution, while the standard deviation dictates its width. In contrast, spatial distribution offers a more intuitive visualization of the variations at different locations.

2.9. Threat Score

In this study, precipitation thresholds of 0.1, 10, 25, 50, 100, and 250 mm were selected, and the 3 h TS (threat score), also known as the Critical Success Index (CSI), was calculated to evaluate whether the time shifts could correct precipitation biases. Since the main precipitation events occurred in Guangdong Province, for the purpose of TS calculation, the subsequent precipitation validation was carried out exclusively within the Guangdong Province region. A higher TS value indicated greater forecast accuracy, and the closer the TS was to 1, the higher the forecast accuracy.

The formula for the TS is defined as follows:

$$TS = \frac{H}{H + F + M} \quad (4)$$

where H represents the number of hits, which refers to instances where precipitation was both forecasted and occurred; F represents the number of false alarms, which refers to instances where precipitation was forecasted but did not occur; and M represents the number of misses, which refers to instances where precipitation occurred but was not forecasted.

3. Results

3.1. Precipitation Bias

On 20 October 2023, heavy rainfall occurred in Guangdong, Guangxi, and the surrounding areas under the influence of Typhoon Sanba. From 0000 UTC on the 19th to 2200 UTC on the 20th, extremely heavy rainfall amounts of 250–450 mm were observed in areas such as Maoming, Zhanjiang, and Yangjiang in Guangdong, with some localities in Beihai exceeding 500 mm (according to the Central Weather Bureau: Weather Bulletin). Radar reflectivity at 0000 UTC on the 20th shows that areas with reflectivity values above 35 dBZ are concentrated in western Guangdong and eastern Guangxi, indicating heavy precipitation in these regions. Reflectivity values between 15 and 35 dBZ were mainly observed in southern Hunan and parts of Fujian, where the precipitation intensity was relatively weak (Figure 2).

On 30 April 2024, heavy rainfall and strong convection occurred in Jiangnan and South China. Between 1600 UTC and 2200 UTC on 29 April, squall lines formed from northern Guangxi to northern Fujian and continued moving southeastward due to pressure gradients. From 0000 UTC on April 30 to 0000 UTC on 1 May, most of Zhejiang, southern

Jiangxi, central and southern Fujian, eastern Guangxi, and north–central Guangdong experienced heavy to torrential rainfall. In southern Fujian and northern Guangdong, rainfall ranged from 100 to 180 mm, with some areas experiencing short-term intense precipitation (maximum hourly rainfall of 30–60 mm, occasionally exceeding 80 mm in certain locations) (according to the Central Weather Bureau: Weather Bulletin). Radar reflectivity at 0224 UTC on April 30 shows that areas with reflectivity values above 35 dBZ were concentrated in the southeastern coastal regions of Guangdong and Fujian, while the precipitation intensity in areas such as Jiangxi and Hubei was relatively weak (Figure 2).

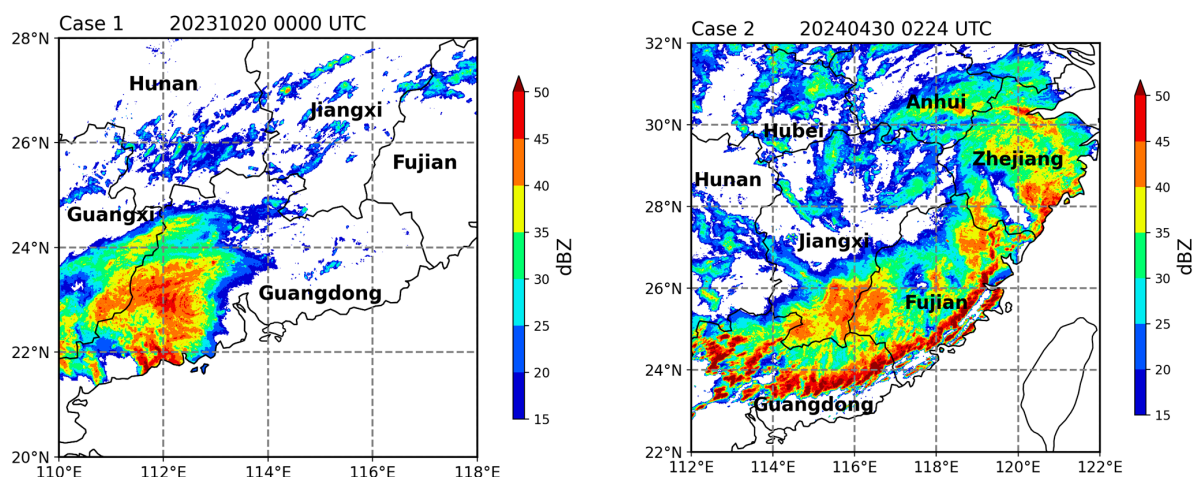


Figure 2. Radar composite reflectivity.

Figure 3 shows the spatial distribution of observed precipitation (from the CMPAS precipitation fusion product) and simulated precipitation (from the CMA-MESO model) in East and South China during the periods of 0000–0100 UTC on 20 October 2023 (Case 1) and 0200–0300 UTC on 30 April 2024 (Case 2). In Case 1, the observed heavy precipitation is mainly concentrated in the southern part of Guangdong Province and along its coastal areas, with rainfall exceeding 20 mm and a relatively wide coverage. Additionally, smaller areas of rainfall are observed in Guangxi, Jiangxi, and Hunan. Although the simulation also predicted the main precipitation area, there were differences in both the intensity and distribution of precipitation compared to the observed results. The simulated heavy rainfall area is more concentrated in the southwest of Guangdong, which does not correspond well to the actual observed precipitation. In Case 2, the observed heavy precipitation is mainly concentrated in the southeastern coastal regions, with a wide coverage, especially in the coastal areas of Guangdong and Fujian provinces. In contrast, the simulation result is significantly more inland, with notable differences in both the intensity and distribution of precipitation compared to the observed data. Comparing the spatial distribution of observed and simulated precipitation for both cases, it is evident that there are certain deviations in both precipitation events, particularly in Case 2, where the forecasted precipitation appears to be clearly delayed.

3.2. Optimal Time-Shifted NWP Model

To explore the potential of high-temporal-resolution visible data from geostationary satellites in correcting forecast-time biases in the two aforementioned cases, this study employs a time-shifting method to analyze the correlation between observed albedo at fixed times (20 October 2023, 0000 UTC, and 30 April 2024, 0220 UTC) and simulated albedo at different times (Figure 4). Through correlation analysis, we identify the simulated time most strongly correlated with the observed albedo. We hypothesize that when the difference between simulated and observed albedo is minimized—i.e., when the simulated and

observed albedo are closest at each grid point, corresponding to the maximum correlation—this time aligns with the actual observation time, enabling forecast timing correction.

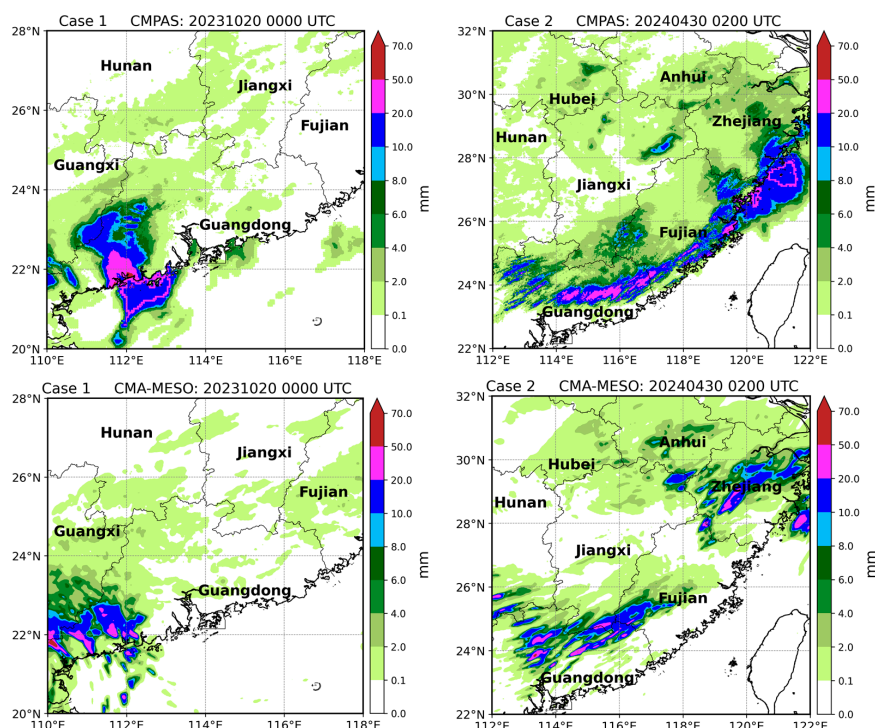


Figure 3. The spatial distribution of 1 h accumulated observed precipitation (up) and simulated precipitation (down).

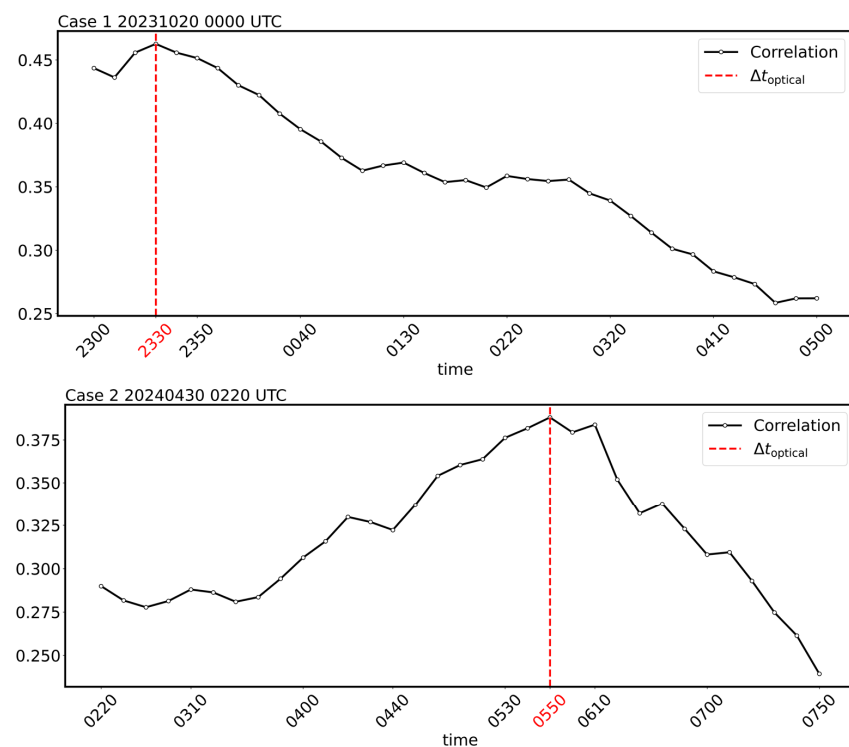


Figure 4. The correlations between the measured albedo at the fixed times of 0000 UTC on 20 October 2023 and 0220 UTC on 30 April 2024 and the simulated albedo at various times. Due to the unavailability of satellite observation data, the data for 0240 UTC on 20 October 2023 and 0240 UTC on 30 April 2024 were excluded from the analysis.

Since visible reflectance data are only available during the day, and the solar zenith angle is low before 0700 UTC, a 6 h time window from 2300 UTC on 19 October 2023, to 0500 UTC on 20 October 2023, was selected for Case 1 in order to maximize the search space and make optimal use of the available data. The correlation between simulated albedo at different times and the observed albedo at the fixed time (20 October, 0000 UTC) was then analyzed. The figure shows that the simulated albedo at 2330 UTC on 19 October 2023, exhibits the highest correlation with the observed albedo at 0000 UTC on 20 October 2023, with a correlation coefficient of 0.463. Considering that the correlation may be influenced by similarities in cloud shape, size, and position, we inferred that the forecast tends to be too early. Thus, we recommend adjusting the forecast forward by 30 min to correct the bias. In Case 2, where it is already known that the forecast is biased toward being too slow, the fixed time of 0220 UTC on 30 April 2024, was selected, and a time window from 0220 UTC to 0820 UTC on 30 April 2024, was used for analysis. The figure shows that the simulated albedo at 0550 UTC on 30 April 2024, exhibits the highest correlation with the observed albedo at 0220 UTC, with a correlation coefficient of 0.388. Therefore, we suggest adjusting the forecast backward by 3 h and 30 min to correct this bias.

Figure 5 shows the spatial distribution of measured albedo data from the CH03 channel of the Himawari-9/AHI, alongside simulated data before and after time-shift adjustments. The first row depicts the measured albedo data, the second row shows the simulated albedo data at the time of the measurements, and the third row presents the simulated albedo data after the time-shift adjustment. In Case 1, the position of the cloud map changed minimally before and after the time shift and aligned with the measured cloud map. This is attributed to the influence of cold air moving southward on the northern side and Typhoon Sanba on the southern side, which caused the position of the cloud tops to remain nearly unchanged, remaining concentrated over Guangdong Province and other regions of southern China. In Case 2, the progression of the measured cloud map was considerably faster than that of the simulation, with the cloud layer already extending to coastal areas such as Guangdong and Fujian, while the simulated cloud map remained inland. After the time-shift adjustment, the simulated cloud top position aligned with the actual situation, thereby correcting the cloud position in the simulation.

3.3. Error Analysis

To further investigate the role of the time-shift method in correcting cloud biases, this study examines the PDF and spatial distribution of the OMB before and after the time shift, as shown in Figure 6. In Case 1, the mean OMB before the time shift is 0, with a standard deviation of 0.06. After the time shift, the mean OMB increases to 0.08, while the standard deviation decreases to 0.05. This suggests that although the standard deviation of the bias is reduced during the time-shifting process, a degree of systematic bias is introduced. Regarding spatial distribution, the bias before the time shift exhibits a relatively uniform spatial distribution, with both positive and negative deviations and relatively small bias values. After the time shift, the deviations are predominantly positive. In Case 2, the mean OMB before the time shift is 0.04, with a standard deviation of 0.18. After the time shift, the mean OMB decreases to 0, and the standard deviation reduces to 0.16. This indicates that both the mean and standard deviation of the OMB are reduced following the time shift. In terms of spatial distribution, the spatial homogeneity of the bias improves after the time shift, with an overall reduction in bias, particularly in the coastal areas along the Guangdong–Fujian border.

Errors are significantly larger under cloudy or precipitating conditions compared to clear skies, often arising from deficiencies in the forecast model. In particular, forecast errors related to humidity, clouds, and precipitation tend to be larger than those related to dy-

namical variables such as temperature or potential. Furthermore, radiative transfer models exhibit greater errors under cloudy and rainy conditions than under clear skies [20,34,35]. Geer et al., noted that discrepancies between brightness temperatures simulated by the RTTOV model and observed values result not only from errors in the RTTOV model itself but also from inaccuracies in cloud water and cloud ice data simulated by the NWP model [36]. The limited predictability of small-scale clouds and precipitation in NWP models often impacts the error budget in model–observation comparisons, especially with regard to imperfections in the shape, size, and intensity of clouds and precipitation. In addition to errors in the model and RTTOV simulations, aerosols can also affect cloud simulations. While molecular absorption at the 0.64 μm wavelength is negligible, the overall effect of aerosols on reflectance is expected to be small, less than 2% [11].

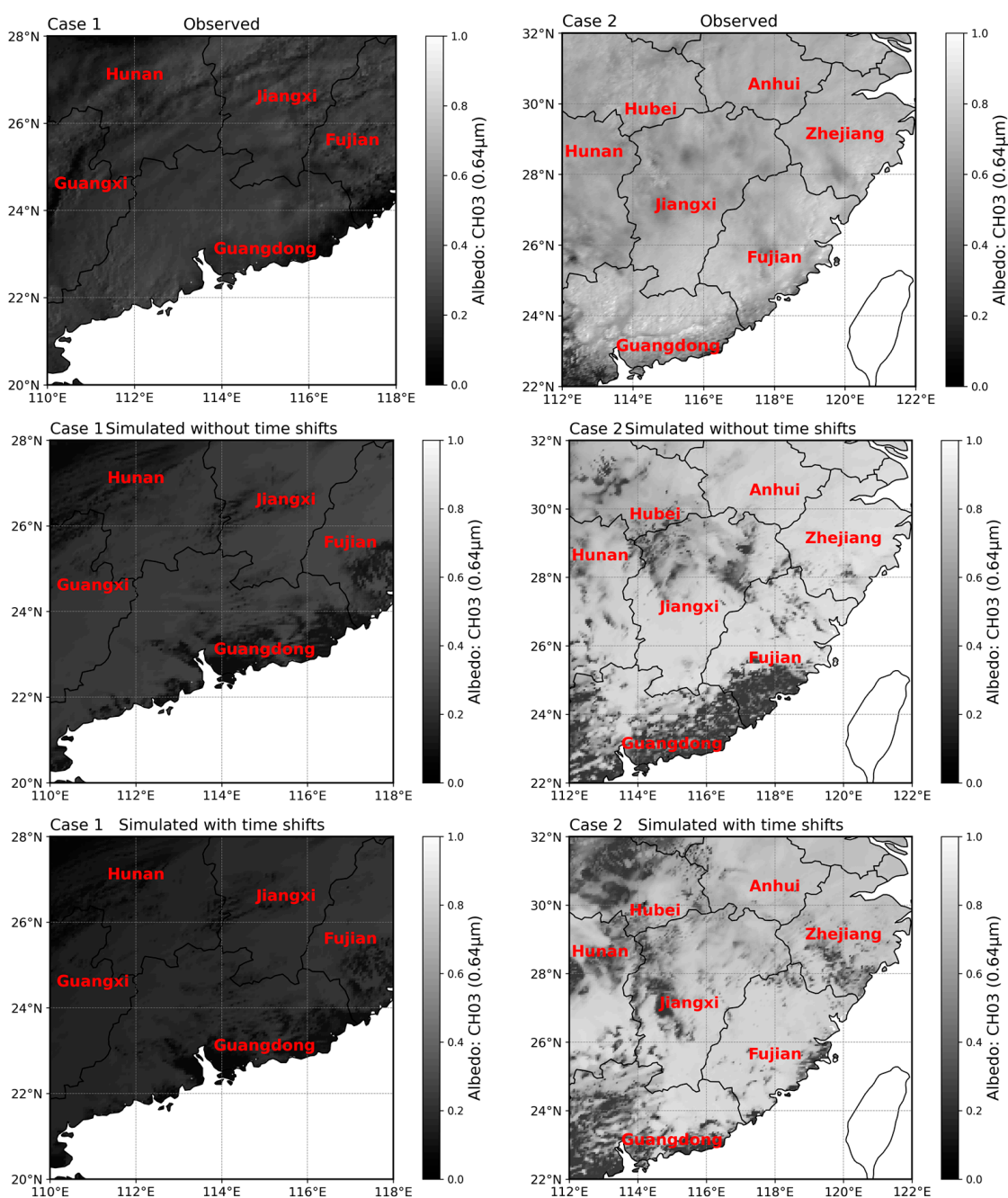


Figure 5. Spatial distribution of observed reflectance data and modeled data before and after time shifts.

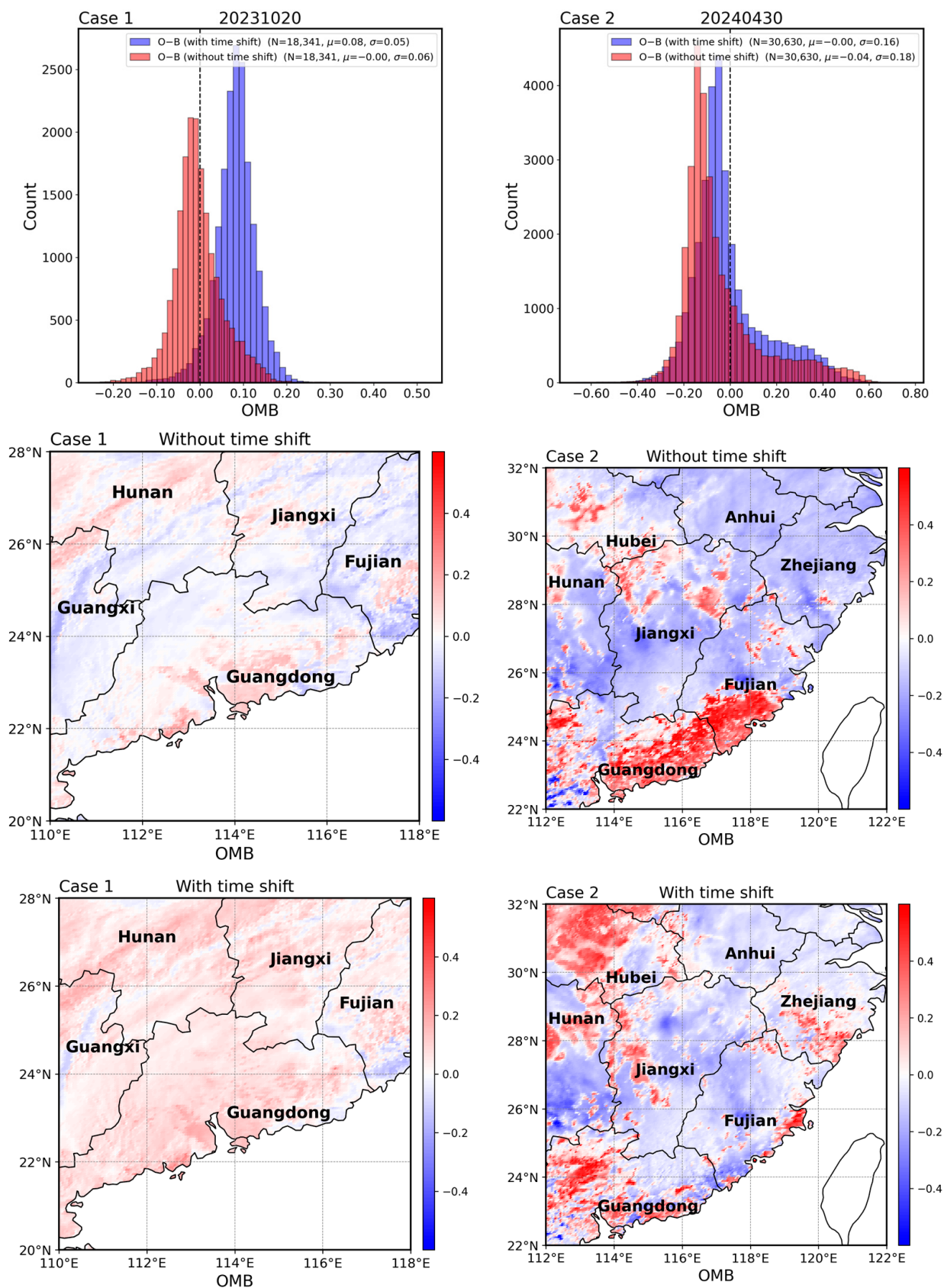


Figure 6. Spatial and PDF distribution of OMB (reflectance) before and after time shifts.

The simulated data used in this study are derived from biased CMA-MESO model forecasts, with additional errors arising from the radiation transfer model calculations. As a result, this study primarily focuses on the changes in bias before and after the time

shifts, rather than on the specific causes of OMB bias. The results show that the time-shift method can partially mitigate cloud biases. However, precipitation is a complex process, and merely correcting cloud biases does not fully reflect its impact on precipitation. Thus, the impact of time shifts on precipitation bias warrants further investigation.

3.4. Precipitation TS and Spatial Distribution Analysis

To investigate the impact of the time-shift method on precipitation bias, this study focuses on precipitation data from Guangdong Province between 0000 and 0300 UTC, calculating the three-hour accumulated precipitation threat score, as shown in Figure 7. The threat score quantifies the agreement between the forecasted and observed precipitation, with higher scores indicating greater forecast accuracy. Additionally, Figure 8 illustrates the spatial distribution of the three-hour accumulated precipitation, with the first row corresponding to the observed precipitation, the second row showing the simulated results without time-shift correction, and the third row depicting the simulated results after time-shift correction.

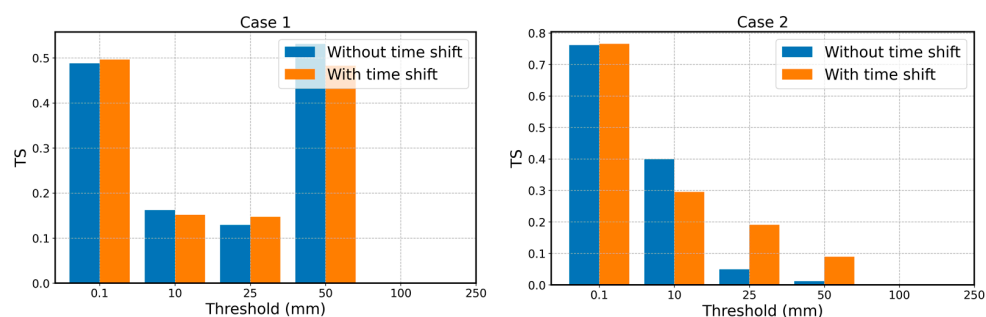


Figure 7. Threat scores for three-hour accumulated precipitation.

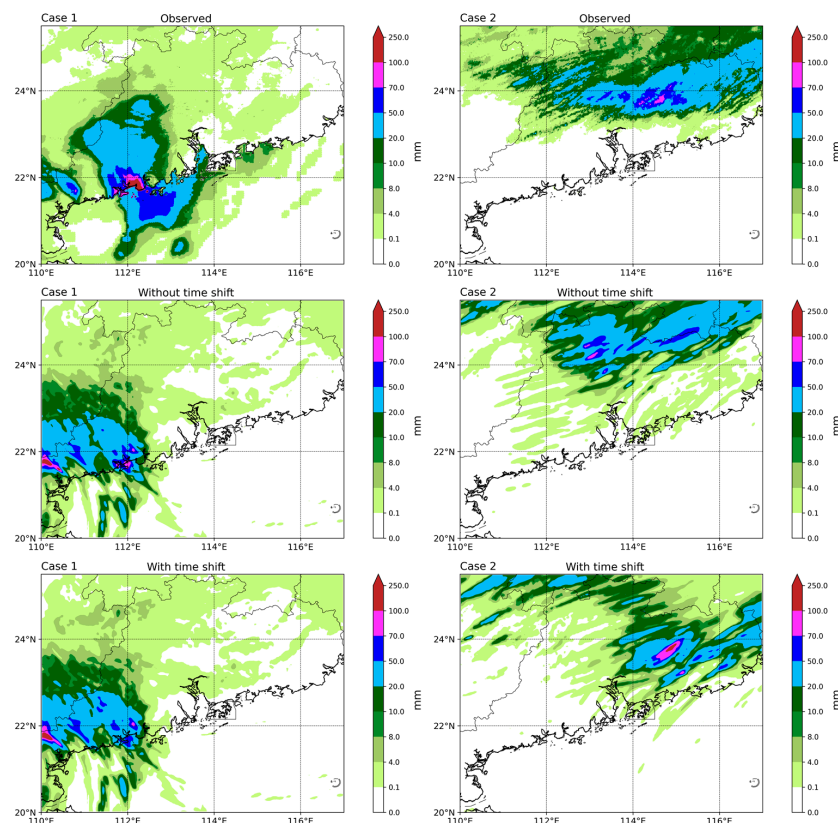


Figure 8. Spatial distribution of three-hour accumulated precipitation.

In Case 1, the impact of the time-shift method varies across different precipitation thresholds. At the 0.1 mm threshold, the TSs before and after the time shift are both close to 0.5, indicating good forecast accuracy at this threshold. At the 10 mm threshold, the threat score before the time shift is 0.162, slightly higher than the score of 0.152 after the time shift. At the 25 mm threshold, the threat score after the time shift is higher than that before. However, at the 50 mm threshold, the threat score before the time shift (0.531) is higher than the post-shift score (0.483). In Case 2, the time-shift method significantly improves forecast accuracy for high-precipitation events. At the 0.1 mm threshold, the threat scores before and after the time shift are both near 0.76, indicating very high forecast accuracy. As the precipitation threshold increases, the threat score gradually decreases. At the 10 mm threshold, the threat score before the time shift is 0.39, slightly higher than the score of 0.30 after the time shift. At both the 25 mm and 50 mm thresholds, the threat score after the time shift is higher than before, though the overall scores are lower, indicating a reduction in forecast accuracy.

From a spatial distribution perspective, the correspondence of precipitation areas in Case 1 before and after the time shift shows limited improvement, primarily due to the combined influence of southward-moving cold air and Typhoon Sanba, which caused the cloud system to persist over Guangdong Province with minimal positional change. As a result, the time-shift method has a relatively limited impact on Case 1. In contrast, in Case 2, the forecast's correspondence with strong precipitation areas improves markedly after the time shift. However, forecast accuracy in medium- and weak-precipitation areas declines, consistent with the trend observed in the threat score. The precipitation maps indicate significant cloud positional deviations in Case 2, with squall lines rapidly moving and exhibiting notable positional shifts. Therefore, the time-shift method exerts a more pronounced corrective effect in Case 2 than in Case 1.

4. Discussion

In weather forecasting, time, intensity, and location are three critical elements. To achieve accurate weather forecasts, all three must be considered simultaneously. However, due to the inherent limitations of NWP models and uncertainties in initial conditions, forecast results often exhibit time biases, with predictions occurring either too early or too late in comparison to actual conditions. This time bias can lead to spatiotemporal discrepancies between observations and model outputs, affecting the reliability of forecasts. Typically, time bias is not discussed separately but is addressed through adjustments to parameterization schemes or data assimilation techniques, which aim to improve the simulation accuracy of precipitation timing, intensity, and location. For example, Ma et al., addressed the complexities of clouds in NWP models by proposing a scale-aware cumulus parameterization scheme and a local cloud fraction and microphysical scheme. They combined the CMA-MESO model (formerly GRAPES-MESO) with multi-source observational data to improve the model's performance in heavy-precipitation forecasting [37]. Similarly, Shen et al., employed the 3DVar data assimilation (DA) method with the WRF model to assimilate radiance from two water vapor channels of the FY-4A satellite in clear-sky conditions, forecasting three typhoon events that made landfall in the western Pacific [38]. Their results showed improved precipitation forecasts and reduced errors in thermal and moisture fields. Wang et al. used the WRF model and the WRFDA system, studying the direct assimilation of three water vapor channel radiance data from the AHI (Advanced Himawari Imager) on the Himawari-8 satellite. They found that the assimilation of satellite data significantly contributed to the relative humidity increments in central Jilin Province, ultimately improving the 3 h precipitation forecast [39]. While these methods enhance precipitation forecast accuracy, they are relatively complex and difficult to implement. As a

result, the time-shifting method has been proposed as a simpler and more effective tool to reduce the time difference between the model and observations, thus improving forecast accuracy. For instance, Gert Mulder et al. [40] used time-shifting to find the best match with InSAR data, showing a 40% reduction in model errors (one sigma) when a weather front was present, with smaller reductions in other situations.

Satellite observations provide high temporal and spatial coverage, offering valuable observational information for high-resolution limited-area models, particularly for data assimilation and model validation. Polar-orbiting satellites typically observe a region no more than twice a day, whereas geostationary satellites can complete full-disk scans every hour, offering higher temporal resolution and broader spatial coverage. This study aims to leverage time-shifting techniques with visible light reflectance data to explore their potential in correcting time biases in NWP. By utilizing the high temporal resolution and wide spatial coverage of geostationary satellites, forecasters can effectively assess and correct time biases in NWP model outputs, improving forecast accuracy. To identify the optimal time-shift moment, we used correlation as the optimization criterion, as it effectively reflects the similarity between observed and simulated data in terms of cloud shape, size, and position. Therefore, the moment with maximum correlation is typically closest to the actual observation time, allowing for an effective correction of forecast times. This method not only improves forecast accuracy but also helps regions better cope with weather events. Despite the time lag between Himawari-9 observational data and the first NC data generation, the time-shifting method still proves effective in utilizing satellite data for evaluation and correction. By comparing available satellite images with adjacent model forecast outputs, forecasters can preliminarily identify whether a time bias exists, making this method valuable even in the presence of time delays.

In this study, we selected two weather phenomena—one with relatively weak movement (Case 1) and the other with more pronounced movement (Case 2)—to compare and illustrate the applicability of the time-shifting method in different scenarios. In Case 1, the interaction between the southward-moving cold air from the north and Typhoon Samba resulted in limited cloud movement, with a relatively small deviation between the forecasted and observed cloud positions. In contrast, Case 2 is characterized by the rapid movement of the cirrus line, a significant positional shift, and large forecast errors, primarily due to the storm line's rapid formation and the numerical weather prediction model's inability to respond in time, leading to delayed forecasts. In this case, applying the time-shifting method adjusted cloud positions—particularly in the precipitation region—thereby improving forecast accuracy. The improvement in the spatial distribution of OMB and the overall PDF distribution in regions such as Guangdong and Fujian (as shown in Figure 6, Case 2) indicates that the time-shifting method can partially correct cloud positions and distributions. Additionally, TS results demonstrate that the precipitation correction effect in Case 2 is significantly better than in Case 1, suggesting that the time-shifting method is particularly effective in mitigating temporal biases in fast-moving precipitation systems. We plan to conduct further analysis using additional data to assess the extent of the correction effect. However, the ability of the time-shifting method to correct cloud positions and precipitation areas is constrained by the fact that visible reflectance data primarily provide information on cloud tops, while precipitation is a complex, multi-level process. It is important to acknowledge the limitations of using visible data for forecast correction. Relying solely on cloud-top heights to estimate precipitation areas can be problematic, especially in processes involving mid- and low-level clouds, where changes in cloud-top heights may not accurately reflect the actual distribution and intensity of precipitation. Adjusting model timing based on observed data may improve performance in some regions, but it could also introduce prediction errors in other areas, leading to spatial and temporal

discrepancies. In future research, we plan to incorporate data from more cases for a more comprehensive evaluation. Applying the methodology throughout the entire forecast cycle, with continuous adjustments at subsequent time points (e.g., 15, 18, 21, and 24 h), will allow for a more thorough assessment of its effectiveness. This will be a key focus of future work. Furthermore, we will explore the nonlinear evolution of weather systems and investigate how the time-shifting method can be adapted to better handle such processes, thereby improving its generalizability and accuracy.

Under cloudy conditions, due to negligible molecular absorption and minimal aerosol impact, the 0.6 μm channel can capture the basic features of clouds. However, it exhibits a low sensitivity to changes in cloud height, primarily reflecting high reflectance from both low-level and high-level clouds, with greater sensitivity to water clouds. This study considers only a single channel, which is relatively simple, and therefore has limitations in analyzing complex cloud systems. Consequently, supplementary analysis using other channels is necessary. Infrared channels can effectively complement visible light data, addressing limitations in cloud height and cloud type identification. For example, radiation at 7.3 μm is highly sensitive to mid-level clouds but less so to low-level clouds [13], while the 1.6 μm channel exhibits higher sensitivity to ice clouds [41], providing detailed information on high-level and ice clouds. Additionally, the cloud-top height data provided by infrared channels aids in analyzing the vertical structure of clouds, supporting more accurate weather forecasts. The combination of visible and infrared data enables a more comprehensive identification and resolution of deficiencies in numerical weather prediction models, such as excessive high-level cirrus clouds, weak shallow convection, excessively strong deep convection, or excessive cloud ice production [20]. Consequently, the integration of multi-channel data not only improves cloud system identification and classification but also aids in more accurate corrections of forecast results for complex weather systems. Future research should focus on integrating multi-channel data (e.g., visible and infrared channels) to improve forecast corrections. Moreover, incorporating high-frequency radar observation data can provide more real-time data for forecasting, particularly in monitoring precipitation and cloud dynamics. By calculating the weights of various variables and applying the time-shift method, more precise bias corrections can be achieved, thus improving the accuracy and reliability of weather forecasts.

5. Conclusions

By applying the time-shift method, we observed a significant improvement in cloud simulation. Specifically, in Case 1, the forecast was improved by shifting it 30 min ahead, while in Case 2, the forecast was delayed by 3 h and 30 min. The time-shift method effectively corrected these forecast-time biases.

An analysis of the PDF and spatial distribution of the OMB biases, both before and after the application of time-shifting, reveals that the method reduces the standard deviation of the biases, enhances spatial homogeneity, and lowers the forecast model error in certain regions. This demonstrates the effectiveness of the time-shift method in correcting cloud biases.

TS results indicate that the time-shift method improves precipitation forecast accuracy, especially when significant movement patterns are involved. A comparison of forecast outcomes in different scenarios clearly shows that the time-shift method can address temporal bias in precipitation predictions within numerical weather prediction models.

Overall, the time-shift method offers a novel approach for addressing time bias in numerical weather prediction models. The study suggests that future research should focus on integrating multichannel data (e.g., visible and infrared) with high-frequency radar observations to further enhance correction accuracy.

Author Contributions: X.S.: Resources, Data Curation, Writing—Original Draft Preparation, Writing—Review and Editing. H.S.: Software, Validation, Methodology. H.W.: Investigation. X.X.: Investigation, Funding Acquisition. W.H.: Conceptualization, Supervision, Project Administration, Funding Acquisition. All authors have read and agreed to the published version of the manuscript.

Funding: This work was funded under the auspices of the National Key Research and Development Program of China (2022YFC3004004) and the National Natural Science Foundation of China (42075155, 42030612).

Data Availability Statement: The radar data are available at <http://idata.cma/cmadaas/> (accessed on 15 June 2024). The NCEP reanalysis data can be found at <http://rda.ucar.edu/datasets/ds083.2/> (accessed on 15 June 2024). The accumulated precipitation was validated by the multi-source observed precipitation products gridded at a 1 km resolution [27]. The Himawari data are available at <http://www.eorc.jaxa.jp/ptree/> (accessed on 10 May 2024).

Acknowledgments: The authors express their gratitude to the China Meteorological Administration for providing the datasets utilized in this study. The authors also sincerely appreciate the insightful comments provided by the anonymous reviewers.

Conflicts of Interest: The authors have no competing interests to declare that are relevant to the content of this article.

Abbreviations

The following abbreviations are used in this manuscript:

AHI	Advanced Himawari Imager
CMPAS	CMA Multi-source Precipitation Analysis System
CREF	Radar Composite Reflectivity
DA	data assimilation
EQR	Equidistant Quadrilateral Projection
GRAPES	Global/Regional Assimilation and Prediction System
JMA	Japan Meteorological Agency
NWP	Numerical weather prediction
OMB	observation-minus-background
PDF	probability density function
RTTOV	TOVS radiation transfer
SAA	satellite azimuth angle
SAZ	satellite zenith angle
SOA	solar azimuth angle
SOZ	solar zenith angle
TS	threat score

References

- Jin, R.; Dai, J.; Zhao, R.; Cao, Y.; Xue, F.; Liu, M.; Zhao, S.; Li, Y.; Wei, Q. Progress and Challenge of Seamless Fine Gridded Weather Forecasting Technology in China. *J. Meteorol.* **2019**, *45*, 445–457.
- Meng, Z.; Zhang, F.; Luo, D.; Tam, Z.; Fang, J.; Sun, J.; Shen, X.; Zhang, Y.; Wang, S.; Han, W.; et al. China's Atmospheric Science Research in the 70 Years since the Founding of New China: The Weather Part. *Sci. Sin.* **2019**, *49*, 1875–1918. [[CrossRef](#)]
- Ma, Z.; Maddy, E.S.; Zhang, B.; Zhu, T.; Boukabara, S.A. Impact Assessment of Himawari-8 AHI Data Assimilation in NCEP GDAS/GFS with GSI. *J. Atmos. Ocean. Technol.* **2017**, *34*, 797–815. [[CrossRef](#)]
- Shen, X.; Wang, J.; Li, Z.; Chen, D.; Gong, J. Research and Operational Development of Numerical Weather Prediction in China. *J. Meteorol. Res.* **2020**, *34*, 19–42. [[CrossRef](#)]
- Tong, H.; Zhang, Y. Diagnosis of precipitation types and its application in the GRAPES-MESO forecasts. *Trans. Atmos. Sci.* **2019**, *42*, 502–512. [[CrossRef](#)]
- Zhang, W.; Kang, L.; Zhou, W.; Yin, H. Extreme Short-time Heavy Precipitation Forecast Based on GRAPES-MESO Model. *J. Arid. Meteorol.* **2021**, *39*, 507–513.

7. Fan, Y.; Chen, L.; Xiao, Z.; Mei, X.; Li, H.; Chen, X. Evaluation of GRAPES-Meso model test for localised heavy rainfall at the edge of the sub-high in the mountainous region of West Hubei, China. *Water Resour. Hydropower Eng.* **2022**, *53*, 7–16. [[CrossRef](#)]
8. Liu, X.; Dong, M.; Qiu, J.; Chen, F. Evaluation of CMA-MESO model for 2020 warm season precipitation forecasting in Zhejiang, China. *J. Zhejiang Meteorol.* **2022**, *43*, 1–11. [[CrossRef](#)]
9. Wan, Z.; Sun, S.; Zhao, B.; Chen, Q. Evaluation and Error Analysis of the July 2021 Extremely Severe Rainstorm in Henan Province Simulated by CMA-MESO Model. *J. Meteorol.* **2024**, *50*, 33–47. [[CrossRef](#)]
10. Lopez, P.; Matricardi, M.; Fielding, M. Validation of IFS+RTTOV/MFASIS solar reflectances against GOES-16 ABI obs. *ECMWF* **2022**, *27*. [[CrossRef](#)]
11. Matricardi, P.L.M. Validation of IFS+RTTOV/MFASIS 0.64- μm reflectances against observations from GOES-16, GOES-17, MSG-4 and Himawari-8. *ECMWF* **2022**, *31*. [[CrossRef](#)]
12. Zhou, Y.; Liu, Y.; Huo, Z.; Li, Y. A preliminary evaluation of FY-4A visible radiance data assimilation by the WRF (ARW v4.1.1)/DART (Manhattan release v9.8.0)-RTTOV (v12.3) system for a tropical storm case. *Geosci. Model Dev.* **2022**, *15*, 7397–7420. [[CrossRef](#)]
13. Kugler, L.; Anderson, J.L.; Weissmann, M. Potential impact of all-sky assimilation of visible and infrared satellite observations compared with radar reflectivity for convective-scale numerical weather prediction. *Q. J. R. Meteorol. Soc.* **2023**, *149*, 3623–3644. [[CrossRef](#)]
14. Roger, S.; James, H.; Emma, T.; Peter, R.; David, R.; Pascal, B.; Jerome, V.; Pascale, R.; Marco, M.; Alan, G. An update on the RTTOV fast radiative transfer model (currently at version 12). *Geoscientific Model Dev.* **2018**, *11*, 2717–2737. [[CrossRef](#)]
15. Scheck, R.M.; Bernhard, M. A fast radiative transfer method for the simulation of visible satellite imagery. *J. Quant. Spectrosc. Radiat. Transf.* **2016**, *175*, 54–67. [[CrossRef](#)]
16. Zhou, Y.; Liu, Y.; Liu, C. A machine learning-based method to account for 3D Short-Wave radiative effects in 1D satellite observation operators. *J. Quant. Spectrosc. Radiat. Transf.* **2021**, *275*, 107891. [[CrossRef](#)]
17. Errico, R.M.; Bauer, P.; Mahfouf, J.F.O. Issues regarding the assimilation of cloud and precipitation data. *Am. Meteorol. Soc.* **2007**, *64*, 3785–3798. [[CrossRef](#)]
18. Schröttele, J.; Weissmann, M.; Scheck, L.; Hutt, A. Assimilating Visible and Infrared Radiances in Idealized Simulations of Deep Convection. *Mon. Weather Rev.* **2020**, *148*, 4357–4375. [[CrossRef](#)]
19. Scheck, L.; Weissmann, M.; Bach, L. Assimilating visible satellite images for convective-scale numerical weather prediction: A case study. *Q. J. R. Meteorol. Soc.* **2020**, *146*, 3165–3186. [[CrossRef](#)]
20. Stefan, G.; Leonhard, S.; Alberto, d.L.; Martin, W. Understanding the model representation of clouds based on visible and infrared satellite observations. *Atmos. Chem. Phys.* **2021**, *21*, 12273–12290. [[CrossRef](#)]
21. Zou, X.; Zhuge, X.; Weng, F. Characterization of Bias of Advanced Himawari Imager Infrared Observations from NWP Background Simulations Using CRTM and RTTOV. *Am. Meteorol. Soc.* **2016**, *33*, 2553–2567. [[CrossRef](#)]
22. Bin, Y.; Chao, L.; Yan, Y.; Peng, Z.; Min, M.; Wei, H. Radiance-Based Evaluation of WRF Cloud Properties Over East Asia: Direct Comparison with FY-2E Observations. *J. Geophys. Res. Atmos.* **2018**, *123*, 4613–4629. [[CrossRef](#)]
23. Li, H.; Wang, X.; Lv, L.; Ma, Y. Refined verification of numerical forecast of subtropical high edge precipitation in Huanghuai Region. *J. Appl. Meteorol. Sci.* **2023**, *34*, 413–425. [[CrossRef](#)]
24. Pan, L.; Liang, M.; Qi, C.; Li, P.; Zhu, Q. Characteristics of meteorological elements and objective forecast verification at the key venues of “the 14th National Games”. *J. Arid. Meteorol.* **2023**, *41*, 491–502.
25. Cai, Y.; Xu, Z.; Gong, X.; Zhong, R.; Huang, G.; Long, H. Evaluation of precipitation forecast of CMA-MESO model in summer of 2021. *J. Arid. Meteorol.* **2023**, *41*, 503–515.
26. Chen, H.; Li, P.; Zhao, Y. A Review and Outlook of Verification and Evaluation of Precipitation Forecast at Convection-Permitting Resolution. *Adv. Meteorol. Sci. Technol.* **2021**, *11*, 155–164. [[CrossRef](#)]
27. Pan, Y.; Gu, J.; Xu, B.; Shen, Y.; Han, S.; Shi, C. Advances in Multi-Source Precipitation Merging Research. *Adv. Meteorol. Sci. Technol.* **2018**, *8*, 143–152. [[CrossRef](#)]
28. Wang, L.; Chen, Q.; Hu, J.; Xu, G. Application of rain and snow phase judgement based on CMA-MESO ice particle content. *J. Appl. Meteorol. Sci.* **2023**, *34*, 655–667. [[CrossRef](#)]
29. Yang, J.; Zhang, Z.; Wei, C.; Lu, F.; Guo, Q. Introducing the New Generation of Chinese Geostationary weather Satellites, Fengyun-4. *Bull. Am. Meteorol. Soc.* **2017**, *98*, 1637–1658. [[CrossRef](#)]
30. Hocking, J.; Vidot, J.; Brunel, P.; Roquet, P.; Lupu, C. A new gas absorption optical depth parameterisation for RTTOV v13. *Geosci. Model Dev.* **2021**, *14*, 2899–2915. [[CrossRef](#)]
31. Mayer, B.; Kylling, A. Technical note: The libRadtran software package for radiative transfer calculations—Description and examples of use. *Atmos. Chem. Phys.* **2005**, *5*, 1855–1877. [[CrossRef](#)]
32. Baran, A.J.; Cotton, R.; Furtado, K.; Havemann, S.; Labonnote, L.C.; Marengo, F.; Smith, A.; Thelen, J.C. A self-consistent scattering model for cirrus. II: The high and low frequencies. *Q. J. R. Meteorol. Soc.* **2013**, *140*, 1039–1057. [[CrossRef](#)]

33. Thompson, G.; Rasmussen, R.M.; Manning, K. Explicit Forecasts of Winter Precipitation Using an Improved Bulk Microphysics Scheme. Part I: Description and Sensitivity Analysis. *Mon. Weather Rev.* **2004**, *132*, 519–542. [[CrossRef](#)]
34. Hobbs, P.V.; Matejka, T.J.; Herzegh, P.H.; Locatelli, J.D.; Houze, R.A. The Mesoscale and Microscale Structure and Organization of Clouds and Precipitation in Midlatitude Cyclones. I: A Case Study of a Cold Front. *J. Atmos. Sci.* **2011**, *37*, 568–596. [[CrossRef](#)]
35. Geng, X.; Min, J.; Yang, C.; Wang, Y.; Xu, D. Analysis of FY-4A AGRI Radiance Data Bias Characteristics and a Correction Experiment. *Chin. J. Atmos. Sci.* **2020**, *44*, 679–694. [[CrossRef](#)]
36. Geer, J.A.; Baordo, F. Improved scattering radiative transfer for frozen hydrometeors at microwave frequencies. *Atmos. Meas. Tech. Discuss.* **2014**, *7*, 1749–1805. [[CrossRef](#)]
37. Ma, Y. Sensitivity Study of Parameter Scheme of Cloud Microphysics Scheme Based on CMA-MESO Model. Master's Thesis, Chinese Academy of Meteorological Sciences, Beijing, China, 2024.
38. Shen, F.; Shu, A.; Liu, Z.; Li, H.; Jiang, L.; Zhang, T.; Xu, D. Assimilating FY-4A AGRI Radiances with a Channel-Sensitive Cloud Detection Scheme for the Analysis and Forecasting of Multiple Typhoons. *Adv. Atmos. Sci.* **2024**, *41*, 937–958. [[CrossRef](#)]
39. Wang, G.; Xu, D.; Jin, M.; Huang, S.; Guo, X. The Application of Assimilating Infrared Radiance Data from Himawari8 Satellite for the Prediction of a Heavy Rainfall in Northeast China. *Desert Oasis Meteorol.* **2024**, 1–14.
40. Mulder, G.; Barkmeijer, J.; Haan, S.d.; Leijen, F.v.; Hanssen, R. On the Use of InSAR for Estimating Timing Errors in Harmonie-Arome Water Vapor Fields. *J. Geophys. Research. Atmos.* **2025**, *130*, e2023JD040566. [[CrossRef](#)]
41. Wolters, E.L.A.; Roebeling, R.A.; Arnout, A.; Feijt, J. Evaluation of Cloud-Phase Retrieval Methods for SEVIRI on Meteosat-8 Using Ground-Based Lidar and Cloud Radar Data. *J. Appl. Meteorol. Climatol.* **2008**, *47*, 1723–1738. [[CrossRef](#)]

Disclaimer/Publisher's Note: The statements, opinions and data contained in all publications are solely those of the individual author(s) and contributor(s) and not of MDPI and/or the editor(s). MDPI and/or the editor(s) disclaim responsibility for any injury to people or property resulting from any ideas, methods, instructions or products referred to in the content.